

A Virtual Acoustic Black Hole on a Cantilever Beam

Samuel Quaegebeur^{a,*}, Ghislain Raze^a, Li Cheng^b, Gaëtan Kerschen^a

^aDepartment of Aerospace and Mechanical Engineering, University of Liège, Allée de la Découverte 9 B-4000 Liège, Belgium

^bDepartment of Mechanical Engineering, The Hong Kong Polytechnic University, Hung Hom Kowloon, Hong Kong SAR, P. R. China

Abstract

An acoustic black hole (ABH) consists of a tapered structure whose thickness follows a power-law profile. When attached to a host structure, an ABH localizes and traps the vibrational energy, which can then be dissipated through, e.g., a damping layer. However, effective vibration mitigation is known to occur only above a cut-on frequency which is inversely proportional to the length of the tapered structure. In this context, the main thrust of this paper is to replace a mechanical ABH by a digital controller so as to create a so-called *virtual acoustic black hole* (VABH), thus, freeing the ABH from possible mechanical constraints (e.g., compactness, manufacturing and fatigue issues). The proposed VABH is first detailed theoretically. The salient features and performance of the VABH are then demonstrated both numerically and experimentally using a cantilever beam as a host structure. Eventually, it is shown that the VABH significantly enlarges the applicability of the concept of an ABH.

Keywords: Acoustic black hole, Active control, Vibration mitigation, Dynamic substructuring

1. Introduction

The acoustic black hole (ABH) effect was first proposed by Mironov in [1]. The mechanical device consists of a tapered wedge beam with a variable thickness following a power-law function. Because the group velocity of a flexural wave is proportional to the square root of the thickness, an acoustic trap with - in principle - no reflection can be achieved through a mechanical device whose tip has a zero thickness. In view of unavoidable manufacturing tolerances, the achievable absorption performance necessarily decreases. To enhance the ABH effect, different strategies were proposed during the last two decades, namely the addition of a damping layer [2, 3] or the use of an extended platform at the end of the tapered beam [4]. The different

*Corresponding author

Email address: squaegebeur@uliege.be (Samuel Quaegebeur)

features of an ABH along with the existing body of literature are explained in detail in the review paper [5].

10 One of the most important parameters is the cut-on frequency above which the ABH starts to be effective. Because this frequency is inversely proportional to the length of the tapered wedge beam, a particularly long and thin ABH is necessary for vibration mitigation at low excitation frequencies (say below 100 Hz). Several hindrances may arise from this feature, e.g., the manufacturing process can be challenging, and the mechanical system can become cumbersome and brittle, as shown in Figure 1. Attempts to obtain a
15 more compact system [6, 7] or to increase the fatigue limits [8] were carried out. Different studies were also conducted to achieve vibration reduction below the cut-on frequency of the system. For instance, references [9, 10] exploit nonlinearities to transfer energy from low to high frequencies where the ABH is known to be effective. Other studies combine the ABH effect with either piezoelectric transducers connected to linear/nonlinear shunt circuits [11, 12, 13] or feedforward/feedback control laws [14, 15, 16]. However,
20 the manufacturing process and the fragility of the ABH still remain important bottlenecks.



(a) Cantilever beam equipped with an ABH.



(b) Close-up at the tip, side view.



(c) Close-up at the tip, front view.

Figure 1: Beam with a 35 cm-long ABH. Due to the small thickness, the tip was crooked during experimental tests.

The present study finds its roots in the recent development of digital vibration absorbers [17, 18, 19, 20]

or energy harvesters [21]. Because a digital controller can synthesize virtually any impedance function (even nonlinear ones [22]), it can advantageously replace analog shunt circuits for piezoelectric vibration absorption [23, 24]. In this paper, we propose the novel concept of a *virtual ABH* (VABH) where the ABH is replaced by a digital controller, see Figure 2. Employing this strategy paves the way for the practical realization of very long and thin ABHs without suffering from the aforementioned mechanical constraints. An interesting, though fundamentally different, study suggesting the use of programmable piezoelectric shunt circuits for mimicking the dynamical characteristics of a mechanical ABH is that of Sugino and co-workers [25]. In their work, the impedance applied to each unit cell is varied so as to control the local dispersion properties of the structure and reproduce the wavelength compression of an ABH.

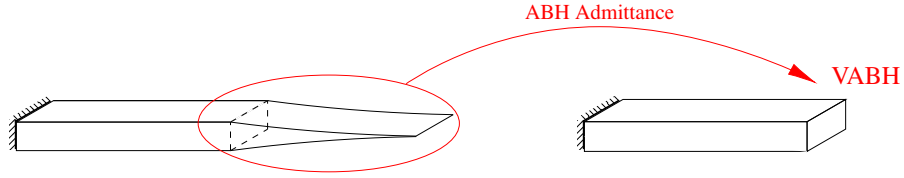


Figure 2: Schematics of the virtual acoustic black hole.

The paper is organized as follows. Section 2 establishes the state space formulation of the ABH effect that will serve as a basis for the feedback control law. The VABH and its salient dynamical features are studied numerically in Section 3. Section 4 discusses the experimental setup and the requirements associated with the VABH. This Section also carries out a correlation with numerical simulations. Section 5 presents the performance of an experimental VABH. Thanks to its virtual nature, ABH with different properties including different materials and lengths can easily be compared. Finally, the conclusions of this study are drawn in Section 6.

2. Formulation of the ABH dynamics as a feedback function

2.1. Finite element modeling

The purpose of this Section is to formulate the ABH effect as a mechanical feedback function. Figure 3 depicts a tapered wedge beam attached to a uniform cantilever beam. The uniform beam is characterized by its material and geometry; h_0 , L and b denote the thickness, length and width, respectively. The tapered wedge beam has a length $L_{ABH} - x_0$, where x_0 corresponds to the tapered wedge beam's truncation. Its width

is equal to b ; its thickness follows the law

$$h(x) = h_0 \left(\frac{L + L_{ABH} - x}{L_{ABH}} \right)^m, x \in [L, L + L_{ABH} - x_0], \quad (1)$$

where m is an integer greater than 1. Due to the truncation x_0 , the tip of the tapered wedge beam has a residual thickness equal to $h_0 \left(\frac{x_0}{L_{ABH}} \right)^m$.

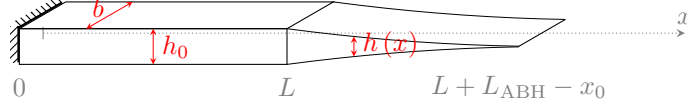


Figure 3: Schematics of the cantilever beam with a tapered wedge profile.

The finite element method is employed to model the coupled system. In what follows, the tapered wedge and cantilever beams are identified with superscripts tb and b, respectively. For both systems, the internal and boundary nodes are denoted by the subscripts I and B, respectively. The equations of motion read

$$\begin{bmatrix} \mathbf{M}_{II}^b & \mathbf{M}_{IB}^b \\ \mathbf{M}_{BI}^b & \mathbf{M}_{BB}^b \end{bmatrix} \begin{bmatrix} \ddot{\mathbf{x}}_I^b \\ \ddot{\mathbf{x}}_B^b \end{bmatrix} + \begin{bmatrix} \mathbf{C}_{II}^b & \mathbf{C}_{IB}^b \\ \mathbf{C}_{BI}^b & \mathbf{C}_{BB}^b \end{bmatrix} \begin{bmatrix} \dot{\mathbf{x}}_I^b \\ \dot{\mathbf{x}}_B^b \end{bmatrix} + \begin{bmatrix} \mathbf{K}_{II}^b & \mathbf{K}_{IB}^b \\ \mathbf{K}_{BI}^b & \mathbf{K}_{BB}^b \end{bmatrix} \begin{bmatrix} \mathbf{x}_I^b \\ \mathbf{x}_B^b \end{bmatrix} = \begin{bmatrix} \mathbf{f}_{\text{ext},I} \\ \mathbf{f}_{\text{ext},B} + \mathbf{f}_{\text{tb} \rightarrow \text{b}} \end{bmatrix} \quad (2a)$$

$$\begin{bmatrix} \mathbf{M}_{II}^{\text{tb}} & \mathbf{M}_{IB}^{\text{tb}} \\ \mathbf{M}_{BI}^{\text{tb}} & \mathbf{M}_{BB}^{\text{tb}} \end{bmatrix} \begin{bmatrix} \ddot{\mathbf{x}}_I^{\text{tb}} \\ \ddot{\mathbf{x}}_B^{\text{tb}} \end{bmatrix} + \begin{bmatrix} \mathbf{C}_{II}^{\text{tb}} & \mathbf{C}_{IB}^{\text{tb}} \\ \mathbf{C}_{BI}^{\text{tb}} & \mathbf{C}_{BB}^{\text{tb}} \end{bmatrix} \begin{bmatrix} \dot{\mathbf{x}}_I^{\text{tb}} \\ \dot{\mathbf{x}}_B^{\text{tb}} \end{bmatrix} + \begin{bmatrix} \mathbf{K}_{II}^{\text{tb}} & \mathbf{K}_{IB}^{\text{tb}} \\ \mathbf{K}_{BI}^{\text{tb}} & \mathbf{K}_{BB}^{\text{tb}} \end{bmatrix} \begin{bmatrix} \mathbf{x}_I^{\text{tb}} \\ \mathbf{x}_B^{\text{tb}} \end{bmatrix} = \begin{bmatrix} \mathbf{0} \\ -\mathbf{f}_{\text{tb} \rightarrow \text{b}} \end{bmatrix}, \quad (2b)$$

where \mathbf{M} , \mathbf{C} , and \mathbf{K} represent the mass, damping and stiffness matrices, respectively. The vector \mathbf{f}_{ext} represents the external forces applied to the cantilever beam. The tapered wedge beam applies forces and torques, $\mathbf{f}_{\text{tb} \rightarrow \text{b}}$, to the cantilever beam. Based on Newton's third law, opposite forces and torques are applied to the tapered wedge beam. If we were to consider the equations of motion of the assembled system, these terms would cancel out. However, our objective is to write the ABH effect generated by the tapered wedge beam as a feedback transfer function. The vector $\mathbf{f}_{\text{tb} \rightarrow \text{b}}$ describes this effect; it thus plays a key role in our analysis.

2.2. State-space formulation

According to control theory, the cantilever beam and ABH are referred to as "plant" and "controller", respectively, as in Figure 4. The equations of motion of the cantilever beam are recast into state-space formulation:

$$\begin{cases} \dot{\mathbf{x}} = \mathbf{E}^b \mathbf{x} + \mathbf{F}^b \mathbf{u} \\ \mathbf{y} = \mathbf{G}^b \mathbf{x} + \mathbf{H}^b \mathbf{u}, \end{cases} \quad (3)$$

The vectors $\mathbf{u} = [\mathbf{f}_{\text{ext},I}^\top, \mathbf{f}_{\text{ext},B}^\top]^\top$, $\mathbf{y} = [\mathbf{x}_I^\top, \dot{\mathbf{x}}_I^\top, \ddot{\mathbf{x}}_I^\top, \mathbf{x}_B^\top, \dot{\mathbf{x}}_B^\top, \ddot{\mathbf{x}}_B^\top]^\top$, and \mathbf{x} represent the input, output and state-space variables, respectively. The state-space matrices are

$$\mathbf{E}^b = \begin{bmatrix} \mathbf{0}_{N_b \times N_b} & \mathbf{I}_{N_b \times N_b} \\ -(\mathbf{M}^b)^{-1} \mathbf{K}^b & -(\mathbf{M}^b)^{-1} \mathbf{C}^b \end{bmatrix}, \mathbf{F}^b = \begin{bmatrix} \mathbf{0}_{N_b \times N_b} \\ (\mathbf{M}^b)^{-1} \end{bmatrix} \quad (4a)$$

$$\mathbf{G}^b = \begin{bmatrix} \mathbf{I}_{N_b \times N_b} & \mathbf{0}_{N_b \times N_b} \\ \mathbf{0}_{N_b \times N_b} & \mathbf{I}_{N_b \times N_b} \\ -(\mathbf{M}^b)^{-1} \mathbf{K}^b & -(\mathbf{M}^b)^{-1} \mathbf{C}^b \end{bmatrix}, \mathbf{H}^b = \begin{bmatrix} \mathbf{0}_{N_b \times N_b} \\ \mathbf{0}_{N_b \times N_b} \\ (\mathbf{M}^b)^{-1} \end{bmatrix} \quad (4b)$$

where N_b denotes the number of degrees of freedom of the cantilever beam.

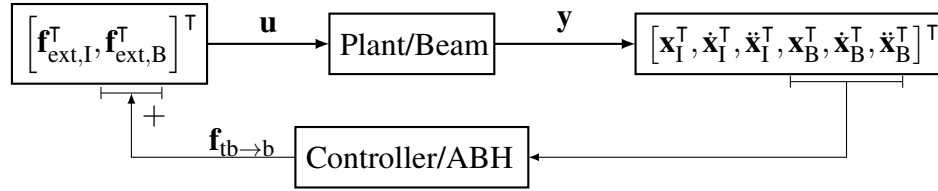


Figure 4: Representation of beam/ABH system with a feedback diagram.

To use the tapered wedge beam as a feedback function, its input vector should contain the displacement \mathbf{x}_B , velocity $\dot{\mathbf{x}}_B$ and acceleration $\ddot{\mathbf{x}}_B$ at the boundary of the beam, and its output should correspond to the forces and torques at the boundary, $\mathbf{f}_{\text{tb} \rightarrow \text{b}}$. The equations of motion of the tapered wedge beam are

$$\begin{cases} \frac{d}{dt} \begin{bmatrix} \mathbf{x}_I^{\text{tb}} \\ \dot{\mathbf{x}}_I^{\text{tb}} \end{bmatrix} = \mathbf{E}^{\text{tb}} \begin{bmatrix} \mathbf{x}_I^{\text{tb}} \\ \dot{\mathbf{x}}_I^{\text{tb}} \end{bmatrix} + \mathbf{F}^{\text{tb}} \begin{bmatrix} \mathbf{x}_B \\ \dot{\mathbf{x}}_B \\ \ddot{\mathbf{x}}_B \end{bmatrix} \\ \mathbf{f}_{\text{tb} \rightarrow \text{b}} = \mathbf{G}^{\text{tb}} \begin{bmatrix} \mathbf{x}_I^{\text{tb}} \\ \dot{\mathbf{x}}_I^{\text{tb}} \end{bmatrix} + \mathbf{H}^{\text{tb}} \begin{bmatrix} \mathbf{x}_B \\ \dot{\mathbf{x}}_B \\ \ddot{\mathbf{x}}_B \end{bmatrix} \end{cases} \quad (5)$$

with

$$\mathbf{E}^{\text{tb}} = \begin{bmatrix} \mathbf{0} & \mathbf{I} \\ -(\mathbf{M}_{\text{II}}^{\text{tb}})^{-1} \mathbf{K}_{\text{II}}^{\text{tb}} & -(\mathbf{M}_{\text{II}}^{\text{tb}})^{-1} \mathbf{C}_{\text{II}}^{\text{tb}} \end{bmatrix}, \mathbf{F}^{\text{tb}} = \begin{bmatrix} \mathbf{0} & \mathbf{0} & \mathbf{0} \\ -(\mathbf{M}_{\text{II}}^{\text{tb}})^{-1} \mathbf{K}_{\text{IB}}^{\text{tb}} & -(\mathbf{M}_{\text{II}}^{\text{tb}})^{-1} \mathbf{C}_{\text{IB}}^{\text{tb}} & -(\mathbf{M}_{\text{II}}^{\text{tb}})^{-1} \mathbf{M}_{\text{IB}}^{\text{tb}} \end{bmatrix} \quad (6a)$$

$$\mathbf{G}^{\text{tb}} = \begin{bmatrix} \mathbf{K}_{\text{BI}}^{\text{tb}} - \mathbf{M}_{\text{BI}}^{\text{tb}} (\mathbf{M}_{\text{II}}^{\text{tb}})^{-1} \mathbf{K}_{\text{II}}^{\text{tb}} & \mathbf{C}_{\text{BI}}^{\text{tb}} - \mathbf{M}_{\text{BI}}^{\text{tb}} (\mathbf{M}_{\text{II}}^{\text{tb}})^{-1} \mathbf{C}_{\text{II}}^{\text{tb}} \end{bmatrix} \quad (6b)$$

$$\mathbf{H}^{\text{tb}} = \begin{bmatrix} \mathbf{K}_{\text{BB}}^{\text{tb}} - \mathbf{M}_{\text{BI}}^{\text{tb}} (\mathbf{M}_{\text{II}}^{\text{tb}})^{-1} \mathbf{K}_{\text{IB}}^{\text{tb}} & \mathbf{C}_{\text{BB}}^{\text{tb}} - \mathbf{M}_{\text{BI}}^{\text{tb}} (\mathbf{M}_{\text{II}}^{\text{tb}})^{-1} \mathbf{C}_{\text{IB}}^{\text{tb}} & \mathbf{M}_{\text{BB}}^{\text{tb}} - \mathbf{M}_{\text{BI}}^{\text{tb}} (\mathbf{M}_{\text{II}}^{\text{tb}})^{-1} \mathbf{M}_{\text{IB}}^{\text{tb}} \end{bmatrix}. \quad (6\text{c})$$

In practice, only one type of output is measured from the plant (either displacement, velocity or acceleration). If the output acceleration is measured (as is the case in this study), the plant velocity and displacement can be obtained through single and double integration, respectively. The state-space model can thus be built as

$$\left\{ \begin{array}{l} \frac{d}{dt} \begin{bmatrix} \mathbf{x}_{\text{I}}^{\text{tb}} \\ \mathbf{x}_{\text{B}} \\ \dot{\mathbf{x}}_{\text{I}}^{\text{tb}} \\ \dot{\mathbf{x}}_{\text{B}} \end{bmatrix} = \mathbf{E}^{\text{tb}} \begin{bmatrix} \mathbf{x}_{\text{I}}^{\text{tb}} \\ \mathbf{x}_{\text{B}} \\ \dot{\mathbf{x}}_{\text{I}}^{\text{tb}} \\ \dot{\mathbf{x}}_{\text{B}} \end{bmatrix} + \mathbf{F}^{\text{tb}} \ddot{\mathbf{x}}_{\text{B}}, \\ \mathbf{f}_{\text{tb} \rightarrow \text{b}} = \mathbf{G}^{\text{tb}} \begin{bmatrix} \mathbf{x}_{\text{I}}^{\text{tb}} \\ \mathbf{x}_{\text{B}} \\ \dot{\mathbf{x}}_{\text{I}}^{\text{tb}} \\ \dot{\mathbf{x}}_{\text{B}} \end{bmatrix} + \mathbf{H}^{\text{tb}} \ddot{\mathbf{x}}_{\text{B}}, \end{array} \right. \quad (7)$$

with

$$\mathbf{E}^{\text{tb}} = \begin{bmatrix} \mathbf{0} & \mathbf{0} & \mathbf{I} & \mathbf{0} \\ \mathbf{0} & \mathbf{0} & \mathbf{0} & \mathbf{I} \\ -(\mathbf{M}_{\text{II}}^{\text{tb}})^{-1} \mathbf{K}_{\text{II}}^{\text{tb}} & -(\mathbf{M}_{\text{II}}^{\text{tb}})^{-1} \mathbf{K}_{\text{IB}}^{\text{tb}} & -(\mathbf{M}_{\text{II}}^{\text{tb}})^{-1} \mathbf{C}_{\text{II}}^{\text{tb}} & -(\mathbf{M}_{\text{II}}^{\text{tb}})^{-1} \mathbf{C}_{\text{IB}}^{\text{tb}} \\ \mathbf{0} & \mathbf{0} & \mathbf{0} & \mathbf{0} \end{bmatrix}, \mathbf{F}^{\text{tb}} = \begin{bmatrix} \mathbf{0} \\ \mathbf{0} \\ -(\mathbf{M}_{\text{II}}^{\text{tb}})^{-1} \mathbf{M}_{\text{IB}}^{\text{tb}} \\ \mathbf{I} \end{bmatrix} \quad (8\text{a})$$

$$\mathbf{G}^{\text{tb}} = \begin{bmatrix} \mathbf{K}_{\text{BI}}^{\text{tb}} - \mathbf{M}_{\text{BI}}^{\text{tb}} (\mathbf{M}_{\text{II}}^{\text{tb}})^{-1} \mathbf{K}_{\text{II}}^{\text{tb}} & \mathbf{K}_{\text{BB}}^{\text{tb}} - \mathbf{M}_{\text{BI}}^{\text{tb}} (\mathbf{M}_{\text{II}}^{\text{tb}})^{-1} \mathbf{K}_{\text{IB}}^{\text{tb}} \\ \mathbf{C}_{\text{BI}}^{\text{tb}} - \mathbf{M}_{\text{BI}}^{\text{tb}} (\mathbf{M}_{\text{II}}^{\text{tb}})^{-1} \mathbf{C}_{\text{II}}^{\text{tb}} & \mathbf{C}_{\text{BB}}^{\text{tb}} - \mathbf{M}_{\text{BI}}^{\text{tb}} (\mathbf{M}_{\text{II}}^{\text{tb}})^{-1} \mathbf{C}_{\text{IB}}^{\text{tb}} \end{bmatrix} \quad (8\text{b})$$

$$\mathbf{H}^{\text{tb}} = \mathbf{M}_{\text{BB}}^{\text{tb}} - \mathbf{M}_{\text{BI}}^{\text{tb}} (\mathbf{M}_{\text{II}}^{\text{tb}})^{-1} \mathbf{M}_{\text{IB}}^{\text{tb}}. \quad (8\text{c})$$

50 Now that both state-space models are created, the state-space model of the full system can be defined by using the ABH formulation as a feedback transfer function.

3. Numerical demonstration of the proposed VABH

3.1. Mechanical model

Euler-Bernoulli assumptions were used for beam modeling. One node comprises three degrees of freedom, namely the horizontal u and vertical v displacements and the rotation ϕ . 400 elements were employed for the uniform beam and 800 for the tapered wedge beam. A uniform damping layer on both sides of either the cantilever beam or the tapered wedge beam was added to the model to dissipate the vibrational energy. The material and geometrical properties for each system are listed in Table 1. The damping matrix of each structure is built such that the considered resonance frequencies have all the same modal damping ratio ξ . Note that the residual thickness at the tip of the tapered wedge beam is very small, i.e., $0.6\mu\text{m}$. Such a system would be very challenging to manufacture and would be very brittle. As mentioned in the Introduction, one of the main features of an ABH is its cut-on frequency, f_{cut} . For the ABH in Table 1, we have [26]

$$f_{\text{cut}} = \frac{h_0}{2\pi L_{\text{ABH}}^2} \sqrt{\frac{40E_{\text{ABH}}}{12\rho_{\text{ABH}}}} = 9\text{Hz}. \quad (9)$$

Parameter	Beam	ABH	Damping layer
Length	$L = 1\text{ m}$	$L_{\text{ABH}} = 1\text{ m}$	$L_{\text{d}} = 1\text{ m}$
Width	$b = 20\text{ mm}$	$b = 20\text{ mm}$	$b = 20\text{ mm}$
Thickness	$h_0 = 6\text{ mm}$	$m = 2, x_0 = 10\text{ mm}$	$h_{\text{d}} = 0.8\text{ mm}$
Young modulus	$E_{\text{b}} = 210\text{ GPa}$	$E_{\text{ABH}} = 210\text{ GPa}$	$E_{\text{d}} = 5\text{ GPa}$
Density	$\rho_{\text{b}} = 7800\text{ kg m}^{-3}$	$\rho_{\text{ABH}} = 7800\text{ kg m}^{-3}$	$\rho_{\text{d}} = 920\text{ kg m}^{-3}$
Modal damping	$\xi_{\text{b}} = 0.05\%$	$\xi_{\text{ABH}} = 0.05\%$	$\xi_{\text{d}} = 3\%$

Table 1: Parameters of the coupled system.

3.2. VABH definition

55 The goal of this paper is to create a VABH according to Figure 4. However, it is difficult to measure experimentally the two accelerations and rotation at the interface and to apply the appropriate forces and torque. As a consequence, we consider here a truncated ABH effect, meaning that only the vertical acceleration \ddot{v}_B is measured and only the vertical force $f_{tb \rightarrow b, v}$ is applied. Such a system is referred to as VABH in the remainder of this paper. Its feedback formulation is schematized in Figure 5.

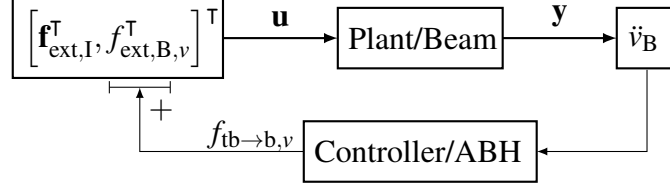


Figure 5: Representation of the VABH as a feedback diagram.

3.3. Numerical results

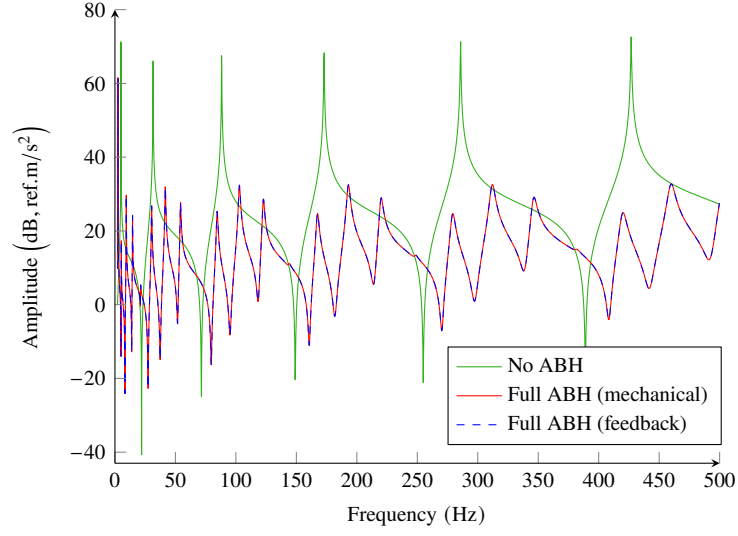
Three different simulations are considered for the purpose of comparison, namely one with no ABH, one with the full ABH (either mechanical or as a feedback transfer function), and one with the VABH. The features expected from a full mechanical ABH are described in different papers, see, e.g., [5, 27]. The system is excited at the tip of the beam. A damping layer is attached to the ABH system. For the case of the uniform beam with no ABH effect, the damping layer is attached to the beam itself.

Figure 6 presents the frequency response functions (FRFs) measured at beam tip. Figure 6(a) confirms the complete equivalence between the mechanical ABH and the ABH defined through the feedback formulation in Figure 4. As expected, the vibration of the beam equipped with the mechanical ABH is significantly reduced for frequencies beyond f_{cut} compared to the case without ABH. Interestingly, the FRF of the VABH beam in Figure 6(b) exhibits performance comparable to that of the mechanical ABH. We stress that this result was obtained for different measurement locations and for different mechanical systems, but this is not further discussed herein for conciseness.

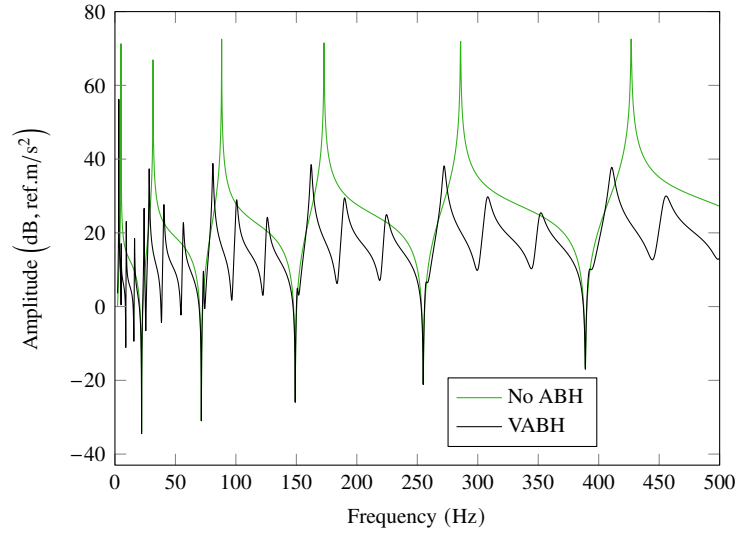
To better highlight the possible differences between the VABH and the standard ABH, several indicators were calculated. Figure 7 displays the reflection coefficient $|R|$ defined based on the experimental technique introduced in [28]. It is equal to one for the uniform beam, because the propagating wave is totally reflected at the boundary. For the full ABH, the reflective coefficient fluctuates along the frequency range as discussed in [28]. Moreover, as the frequency increases, its value tends to decrease as predicted by the geometrical acoustics method [2]. The same trends are observed for the VABH. However, the fluctuation is more pronounced in the case of the VABH.

Figure 8 exhibits the modal damping ratio ξ for the different modes of the considered systems. For the uniform beam upon which a damping layer is attached, the overall damping is around 0.06%. The first mode of both the full ABH and VABH has a frequency around 3 Hz, i.e., below the cut-on frequency. This explains why it exhibits a lower damping ratio around 0.03%. For the higher modes, the damping ratio increases substantially and fluctuates around a value of 0.6%. This increase is also visible for the second

85 mode which is located below the cut-on frequency, but this is consistent with previous observations in the technical literature [5].



(a)



(b)

Figure 6: Frequency response functions measured at beam tip. (a) No ABH and full ABH; (b) no ABH and VABH. The cut-on frequency is represented with the dashed line.

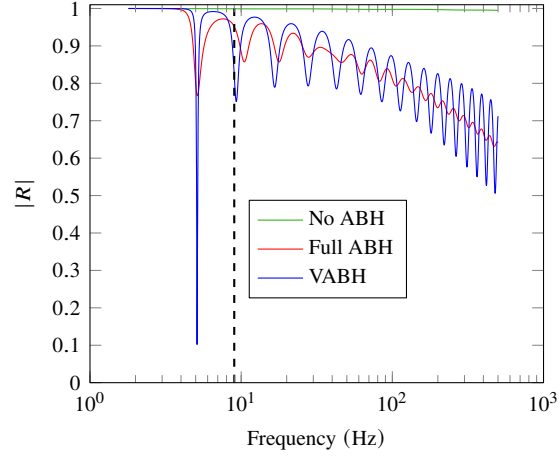


Figure 7: Reflection coefficient $|R|$. The cut-on frequency is represented with the dashed line.

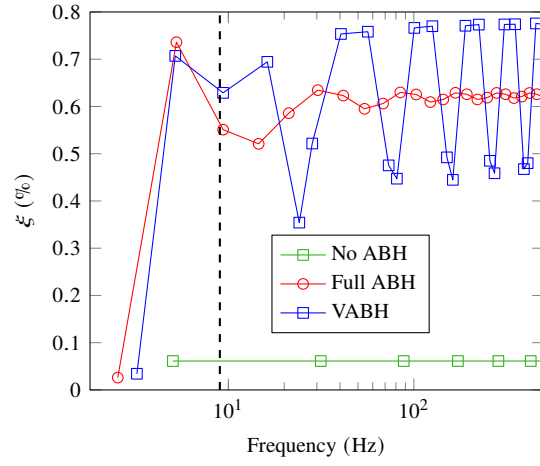


Figure 8: Modal damping ratio ξ . The modes are represented with markers. The cut-on frequency is represented with the dashed line.

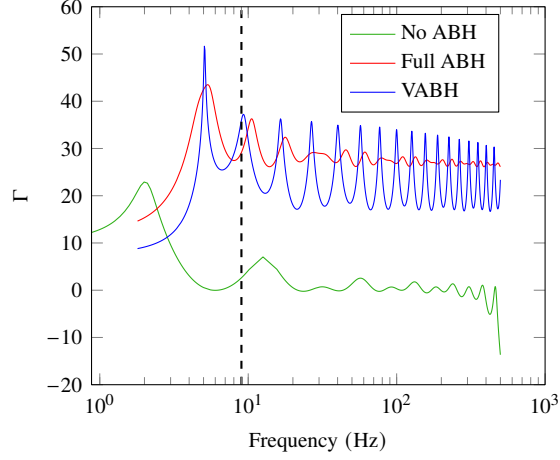


Figure 9: Energy ratio Γ . The cut-on frequency is represented with the dashed line.

Figure 9 compares the energy ratio defined as

$$\Gamma = 10 \log \left(\sqrt{\frac{N_b \sum_{i=N_b+1}^{N_b+N_{tb}} v_i^2}{N_{tb} \sum_{i=1}^{N_b} v_i^2}} \right). \quad (10)$$

It is equal to the ratio of the mean quadratic velocity of the tapered wedge part with respect to that of the uniform beam; it indicates where the energy density is located. For the uniform beam with no ABH, a longer uniform beam is considered with a length equal to $L + L_{ABH}$. For this system, the energy ratio is defined as the quadratic mean velocity of the nodes contained between $[L, L + L_{ABH}]$ with the nodes contained in $[0, L]$. For structures equipped with an ABH, a positive energy ratio is systematically observed. It means that, over the entire frequency range, the energy in the ABH is greater than in the uniform beam. Between 5 Hz and 1000 Hz, the energy ratio of mechanical systems with an ABH is always greater than that of the uniform beam. These results are similar to those in [27]. As for Figures 7 and 8, the VABH presents the same features as the standard ABH but with higher amplitude fluctuations.

In summary, despite the fact that it only considers the vertical acceleration and the vertical interface force, the VABH exhibits performance similar to that of the full ABH system.

4. Experimental considerations

4.1. Experimental setup

The experimental setup, previously employed in [29], is depicted in Figure 10. The uniform rectangular steel cantilever beam has the same parameters as those in Table 1. To avoid friction and contact nonlinearities, the base and the beam were manufactured from one steel block, and the base was bolted to the ground. The system was excited and controlled using the same electrodynamic shaker (TIRA TV51075). A metallic cap with an impedance head of 60 g was attached to the beam.

The excitation signal and the VABH control law were generated with a real-time controller (RTC) DSpace MicroLabBox with a sampling frequency of 100 kHz. The excitation was a multi-sine function in the [0.1 Hz, 500 Hz] frequency interval with an amplitude of 0.01 V. The gain between the command in volt and the applied force is 160 N V^{-1} . The controller, initially written as a state-space system, was transformed into a single input single output (SISO) state-space model. The system was subsequently transformed into a zero-pole-gain function and finally discretized with Tustin's method for implementation into the RTC. Ideally, the controller must be proper and stable to be implemented. To ensure stability, a collocated plant transfer function [30] is almost mandatory, i.e., the sensor and actuator of the feedback function must be located at the same position. The electrodynamic shaker was placed as close as possible from the beam edge (i.e., at 20 mm of the free tip) with an accelerometer glued to it. Overall, the effective moving mass (magnetic coil+accelerometer) is equal to 150 g. To reject undesirable high-frequency shaker dynamics and to have a proper transfer function, a low pass filter

$$h_{\text{LP}} = \frac{\omega_{\text{LP}}^2}{s^2 + \omega_{\text{LP}}s + \omega_{\text{LP}}^2}, \quad (11)$$

was applied to the controller where ω_{LP} is the low-pass cut-on frequency and s is Laplace's variable. The low-pass frequency was set to 800 Hz.

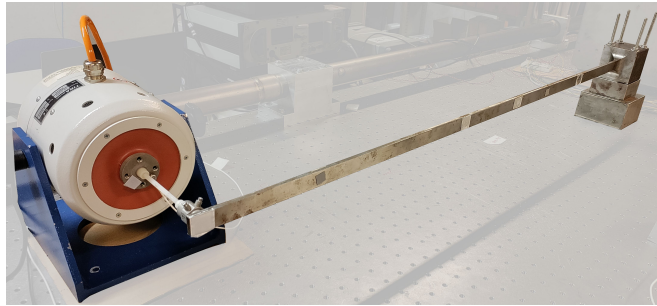


Figure 10: Experimental setup

4.2. Transfer function of the plant

The Bode plot of the experimental setup is provided in Figure 11. The transfer function presents collocated features, i.e., a pole-zero alternation and a phase bounded between -180° and 0° (except at very low frequencies where the accelerometer is no longer measuring accurately). We note that both modes 3 and 10 are in the vicinity of high amplitude modes, which is most likely due to a coupling between the uniform beam and the stinger's dynamics. Modes 6 and 8 present a low amplitude vibration because they correspond to torsional modes. The identified resonance frequencies f_{res} and modal damping coefficients ξ are given in Table 2. The values are different than those in [29] because the measured FRF includes the dynamics of both the stinger and the shaker.

The finite element model was upgraded to account for the presence of the exciting and measurements devices, as illustrated in Figure 12. The transversal mass located at 20mm of the beam tip was updated to account for the impedance head. Besides, a transversal degree of freedom was added to account for the accelerometer and the shaker. It is linked to ground with a stiffness $k_{v,g}$ representing the shaker membrane's stiffness and to the beam by $k_{v,s}$ representing the stinger's stiffness. Measuring the transfer function of the shaker detached from the stinger enabled us to determine that $k_{v,g} = 6.5 \times 10^3 \text{ N m}^{-1}$. The value of the stiffness $k_{v,s}$, $4 \times 10^5 \text{ N m}^{-1}$, was obtained by minimizing the differences between the resonance frequencies of the experimental setup and of the numerical model. In the optimization process, modes 3, 6, 8 and 11 were not retained because they could not be obtained with the finite element model. Overall, an excellent agreement between the experimental and numerical transfer functions can be observed in Figure 11.

Modes	1	2	3	4	5	6	7	8	9	10	11
f_{res} in (Hz)	16.5	31	42.5	81	161.5	249.5	268	311.5	367	408.5	458
ξ (%)	2.65	1.79	NA	0.28	0.41	2.2	0.41	NA	1.91	NA	7.41

Table 2: Resonance frequencies and modal damping coefficients of the experimental setup. NA means that the value could not be identified.

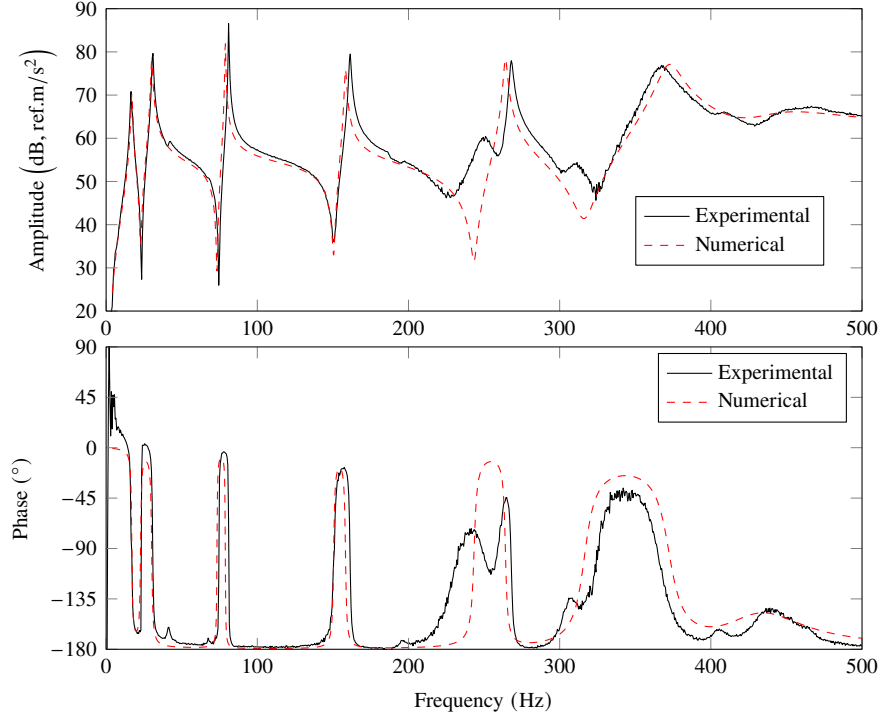


Figure 11: Bode plots of the uniform beam with no VABH.

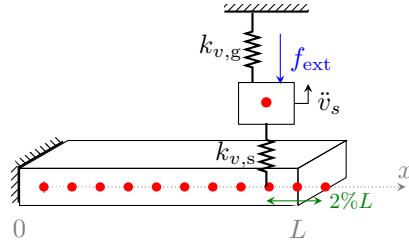


Figure 12: Upgraded finite element model of the beam.

4.3. Open loop system and stability margins

The response of the system with the feedback is called closed-loop transfer function. For a SISO system, it reads

$$T(s) = \frac{P(s)}{1 + P(s)Q(s)}, \quad (12)$$

where P and Q are the transfer functions of the plant and of the controller, respectively. To ensure stability, the roots of the denominator must all have a negative real part. If there exists a frequency ω such

that $1 + P(j\omega)Q(j\omega) = 0$ (with j the unit imaginary number), the closed-loop system possesses a pair of complex conjugate poles on the imaginary axis, i.e., the system is marginally stable. Any perturbation to the nominal system may change their position to either side of the imaginary axis and is thus susceptible to make the controlled system unstable. This happens when the product (also called open-loop transfer function) $P(j\omega)Q(j\omega) = -1$, or equivalently

$$|PQ| = 1, \quad \text{and} \quad \arg(PQ) = \pm 180^\circ, \quad (13)$$

where \arg is the argument of a complex number.

Stability margins are commonly used to quantify how far the open-loop transfer function is from the conditions of Equation 13. The gain margins correspond to the value of $0 - |PQ|$ when $\arg(PQ) = \pm 180^\circ$ and indicate the factor by which the gain in the loop can be increased to make the system marginally stable. Similarly, the phase margins correspond to the value of $\pm 180 - \arg(PQ)$ when $|PQ| \neq 1$ and indicate how robust the system is to delays in the loop. In practice, $40 - 50^\circ$ of stability margins is acceptable [31]. Gain margins should be positive and greater than a few dB.

Figure 13 presents the stability margins for the controller given in Section 3. We note that, instead of inserting a damping layer in the VABH, its modal damping ξ_{ABH} was rather increased up to 5%. To underline the importance of the low pass filter, two open-loop transfer functions are compared that is one with the filter and one without. Beyond the shaker bandwidth around 6kHz, the modes of the shaker are visible. Without the low pass filter, negative gain margin is obtained and thus the closed-loop system would be unstable. However, with the filter, the effect of the shaker is lessened, and stability is ensured. A close-up is shown in Figure 14. We note that phase margins close to -180° do not present a risk to the stability of the system. Indeed, time delays induced by the processor tend to lower the phase of the system and thus increase these phase margins. Similarly, the gain margin of 7.2 dB at 10Hz is expected to be higher during the experiment.

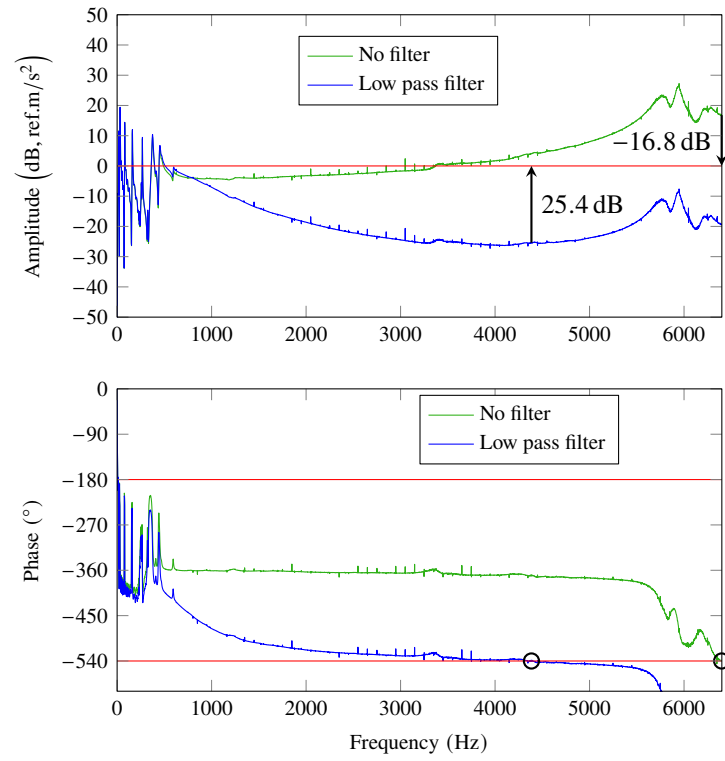


Figure 13: Stability margins of the open-loop system. Only one gain margin is given as an example.

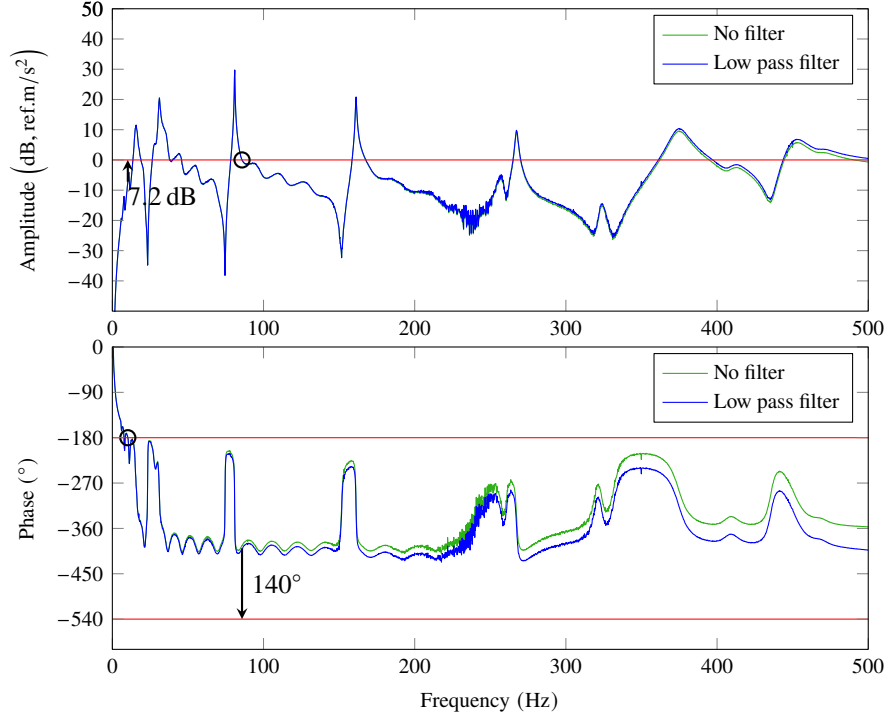


Figure 14: Close-up of Figure 13 in the frequency range of interest.

4.4. Closed-loop system

The fundamental difference between the VABH in Section 3.1 and the experimental VABH comes from the size of the ABH's dynamical model which needs to be reduced substantially. Indeed, the very fine discretization used for the tapered wedge beam model would result in a controller of very high order (number of poles and zeros), which could, in turn, not be handled by the RTC's processor. To preserve the ABH's dynamics and make it digital through the RTC, a Craig-Bampton reduction method [32] was used on the tapered wedge beam. This substructuring approach partitions the degrees of freedom into master and slave degrees of freedom. The former are kept as physical nodes whereas the latter are reduced into N_{CB} generalized control coordinates. In our case, the boundary nodes were kept as master nodes to perform the assembly and $N_{CB} = 20$ was the maximum value allowed by the RTC.

The impact of this model reduction together with the influence of the position of the VABH and of the low-pass filter was studied numerically where the controller corresponds to the one used in Section 4.3. Figure 15 compares a VABH applied directly at the tip (in red) with one located at the shaker's position

(in blue). For the first four modes, the VABH at the tip presents slightly better vibration reduction. For frequencies greater than 280Hz, the VABH placed at the shaker exhibits better performance. Surprisingly, the VABH at the tip shows greater vibration amplitudes than those of the plant in the range [300Hz, 370Hz]. This result comes from the stiffness of the stinger $k_{v,s}$, which, combined with the ABH placed at the tip, creates a number of resonant frequencies in [300Hz, 370Hz]. We note that the modification of the position of an ABH was studied in detail in [7].

Figure 16 plots the influence of the low pass-filter on the FRF (blue vs. green). For low-frequency modes, ω_{LP} is high enough so that the filter has no influence. For the modes at 268Hz and 367Hz, vibration reduction is slightly enhanced with the filter.

Finally, Figure 16 presents the influence of the reduction strategy (green vs. yellow). Except for small discrepancies for the higher modes, keeping 20 modes in the basis does not modify the FRF to a great extent.

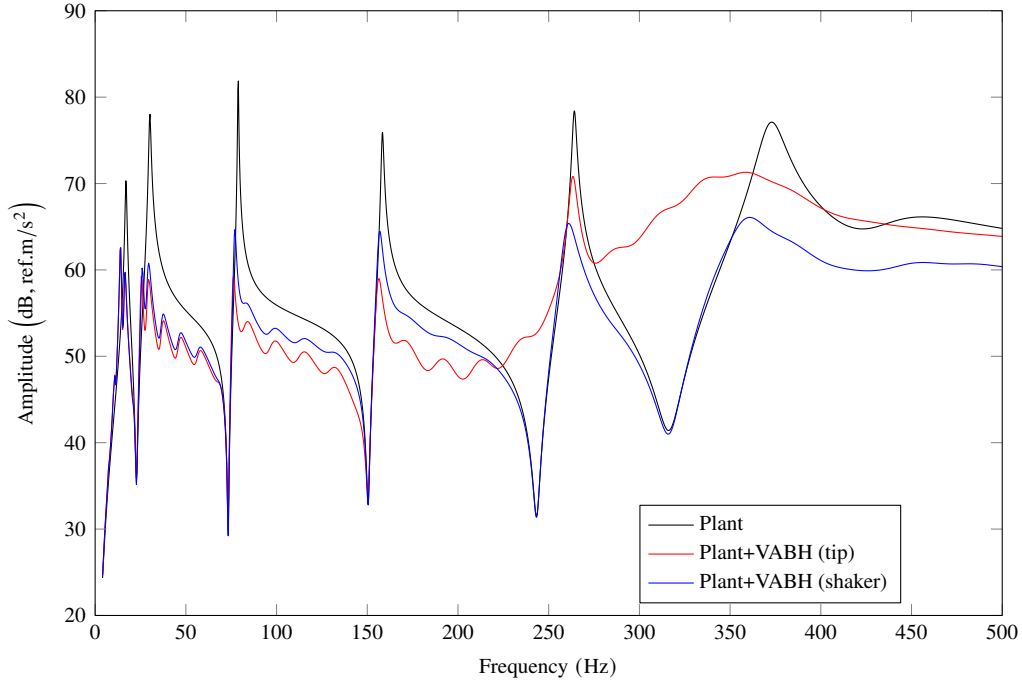


Figure 15: Influence of ABH location on the FRF (numerical result).

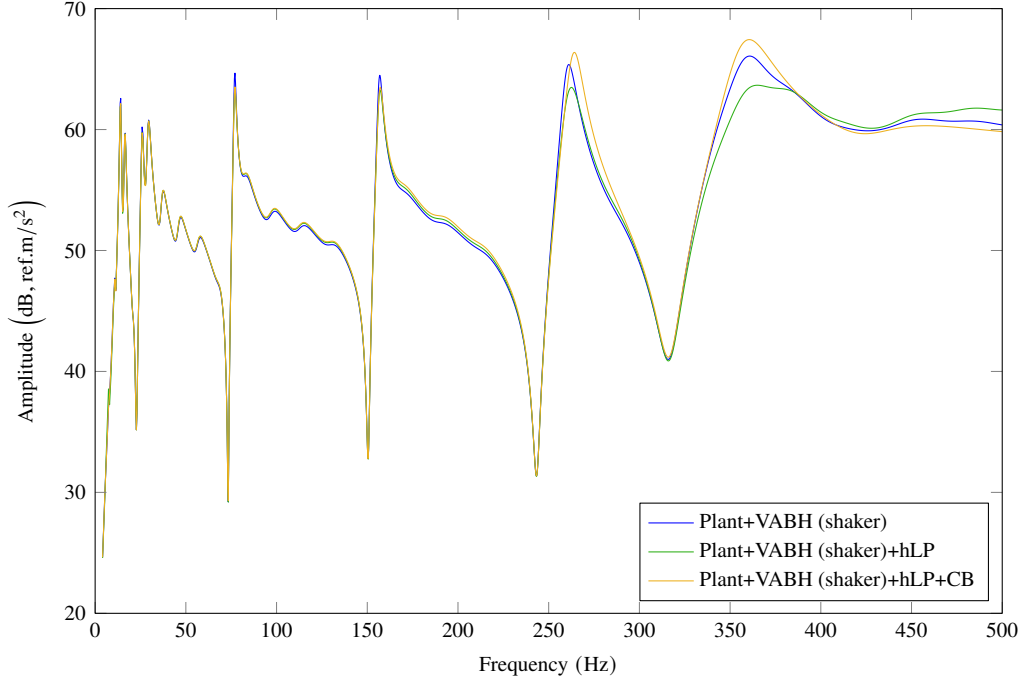


Figure 16: Influence of the filtering and model reduction on the FRF (numerical result).

5. Experimental performances of the VABH

5.1. Nominal VABH

The plant+VABH system is now considered experimentally. The nominal VABH is described by the parameters in Table 1 with $\xi_{ABH} = 5\%$. Figure 17 presents, for the first time, the implementation of a VABH on an experimental setup. The attenuation provided by the VABH is given in Table 3 for different resonance frequencies of the plant. With the exception of the first mode, all modes are significantly damped with the greatest attenuation amounting to 23.9 dB. Thus, excellent attenuation performance is offered by the VABH. These results are also well-predicted by the numerical model, as exemplified in Figure 18.

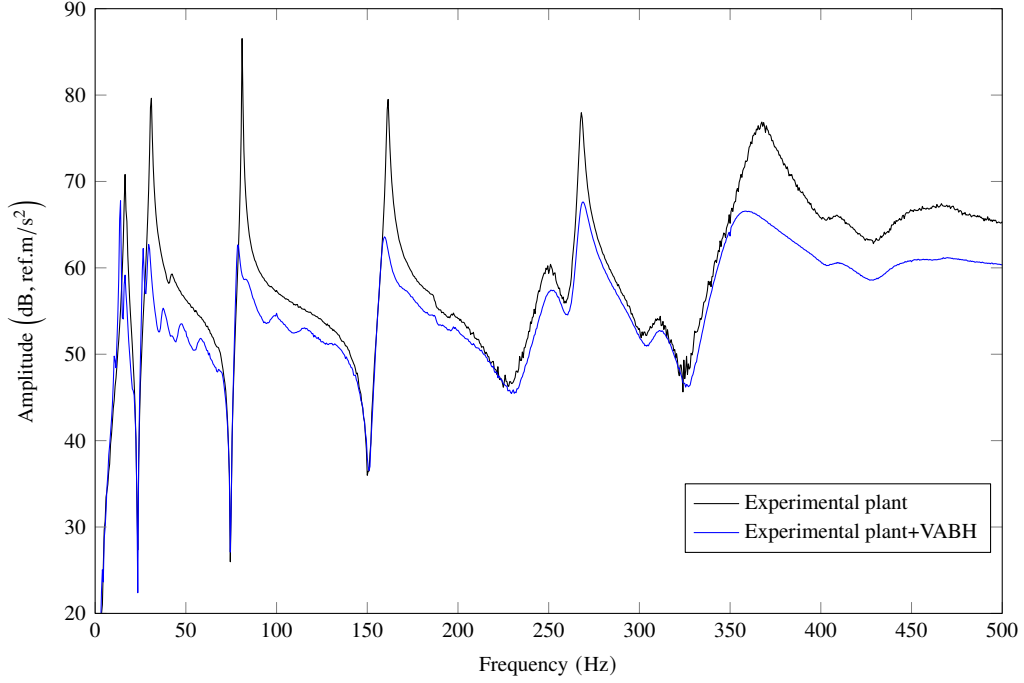


Figure 17: Experimental FRF of the plant and of the plant+VABH system.

Experimental plant modes	1	2	4	5	7	9	11
Experimental attenuation	3	17.4	23.9	15.9	10.3	10.3	6.2
Numerical attenuation	8	17.1	15.4	11.8	12.1	9.7	5.8

Table 3: Attenuation (in dB) of the plant's resonance peaks using the VABH (20 modes). Modes 3, 6, 8, and 10 are excluded, because they correspond to low-amplitude vibration modes.

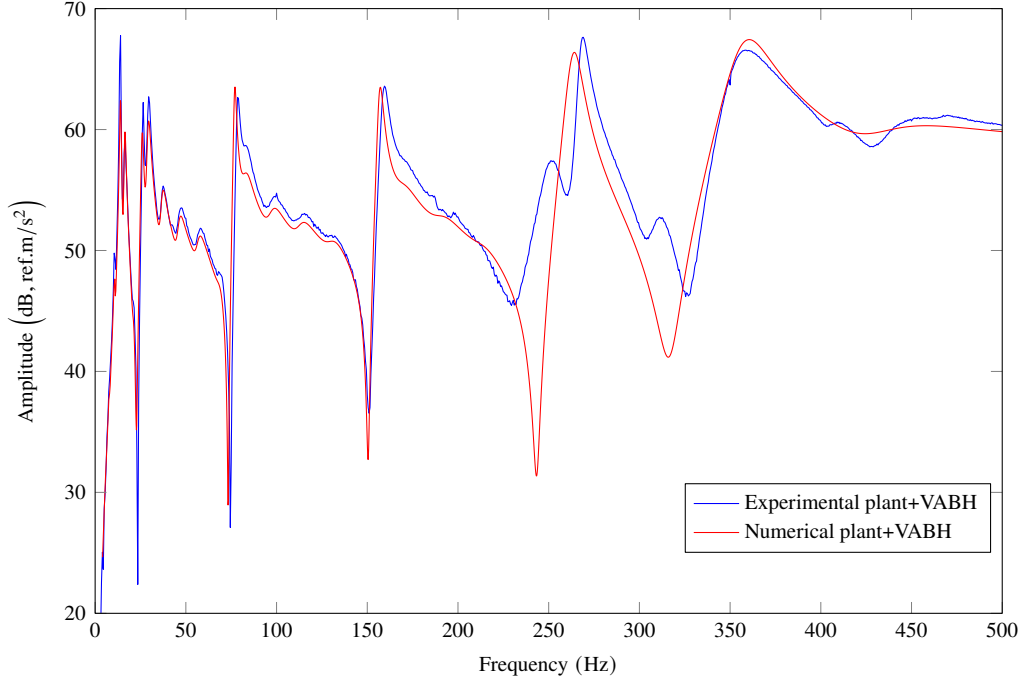


Figure 18: Comparison between experimental and numerical FRFs of the plant+VABH system.

175 5.2. Parametric studies

Because the VABH relies entirely on a microcontroller, changing parameters such as the length or the material of the ABH can easily be carried out. As it will be shown, better performance compared to that of the nominal ABH can be obtained.

180 The influence of the number of modes kept during the Craig-Bampton reduction is first studied in Figure 19. When the reduction is performed with a smaller number of modes, the VABH performance decreases at low frequencies and increases for higher-frequency modes. This latter observation was not expected and should be interpreted with care because the dynamics of the ABH is not well described at high frequencies. In the next experiments, the controller is always implemented with 20 modes.

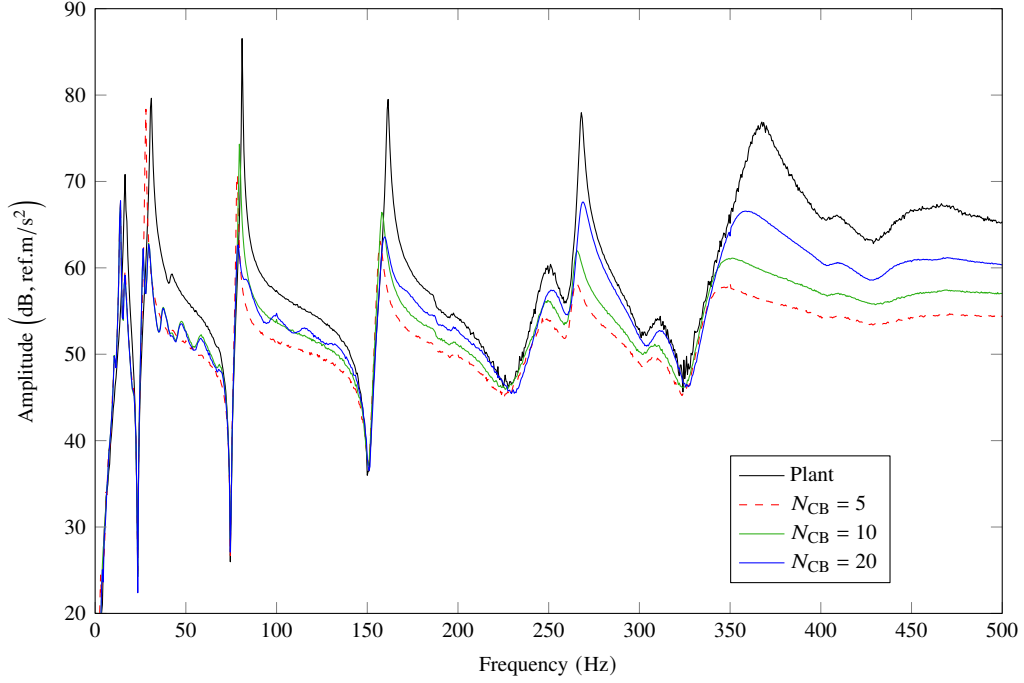


Figure 19: Influence of the number of Craig-Bampton modes kept during model reduction on ABH performance.

Three values of the damping ratio ξ_{ABH} , namely 0.5%, 5%, and 50% are considered in Figure 20. When $\xi_{ABH} = 0.5\%$, the VABH is not very effective as all resonance peaks present fairly high amplitudes. Setting ξ_{ABH} to = 50% reduces substantially the amplitudes of all resonance peaks. A 10dB attenuation is now obtained for the first resonance peak of the plant.

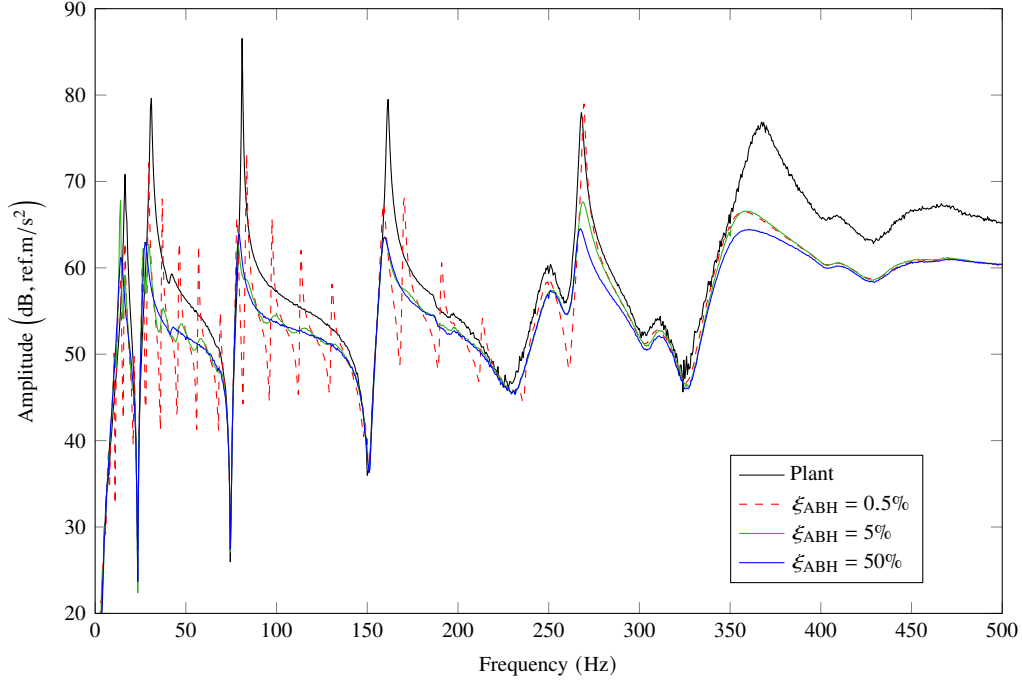


Figure 20: Influence of the modal damping on ABH performance.

Next, the length L_{ABH} is set to either 10mm, 1000mm, or 2000mm in Figure 21. Modifying the length changes the cut-on frequency f_{cut} above which the ABH becomes effective. It is equal to 86kHz, 8.6Hz and 2.15Hz, respectively. For 10mm, the response amplitude is somewhat greater than the plant amplitude at low frequencies. This feature was already observed in Figure 8; the ABH system had a lower modal damping than the cantilever beam for the first mode. Beyond 350Hz, vibration reduction is achieved but should rather be attributed to the low-pass filter and the Craig-Bampton reduction. For the longest ABH beam, the resonance amplitude of all modes is further reduced compared to the nominal case. This is especially true for the first mode whose attenuation amounts to 9dB. A 3000mm-long VABH was also tested successfully but did not exhibit better performance than the 2000mm-long ABH.

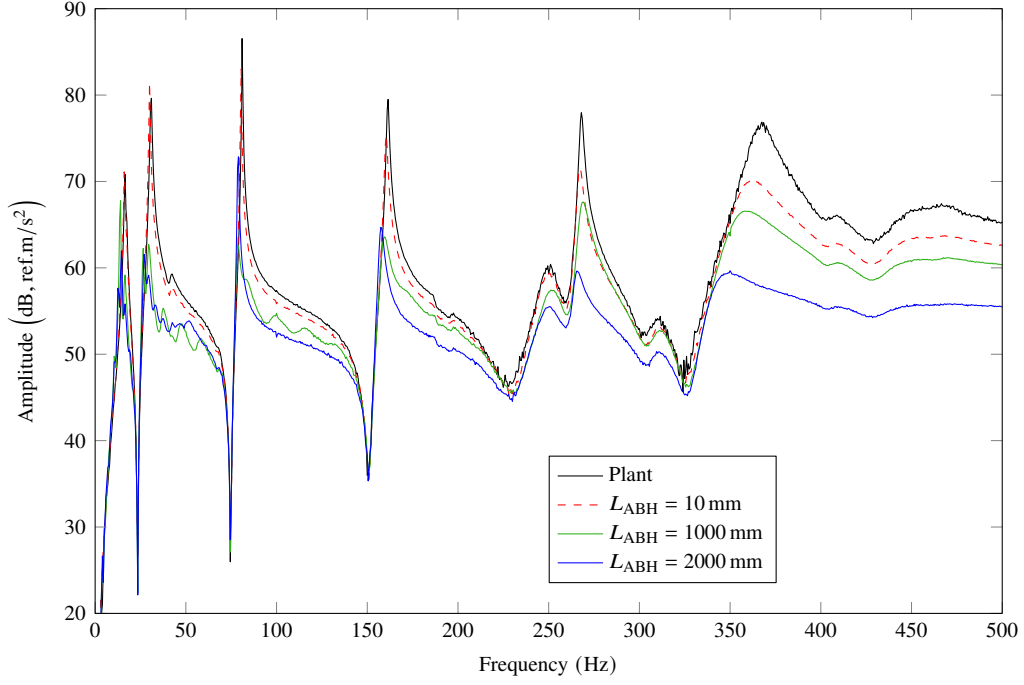


Figure 21: Influence of the ABH length on ABH performance.

Finally, three values of Young's modulus of the tapered wedge beam E_{ABH} are considered in Figure 22, namely 2.1 GPa, 210 GPa, and 21 TPa. For the greatest value, extremely good vibration attenuation is observed for all modes. In this case, the first mode is attenuated by 11 dB.

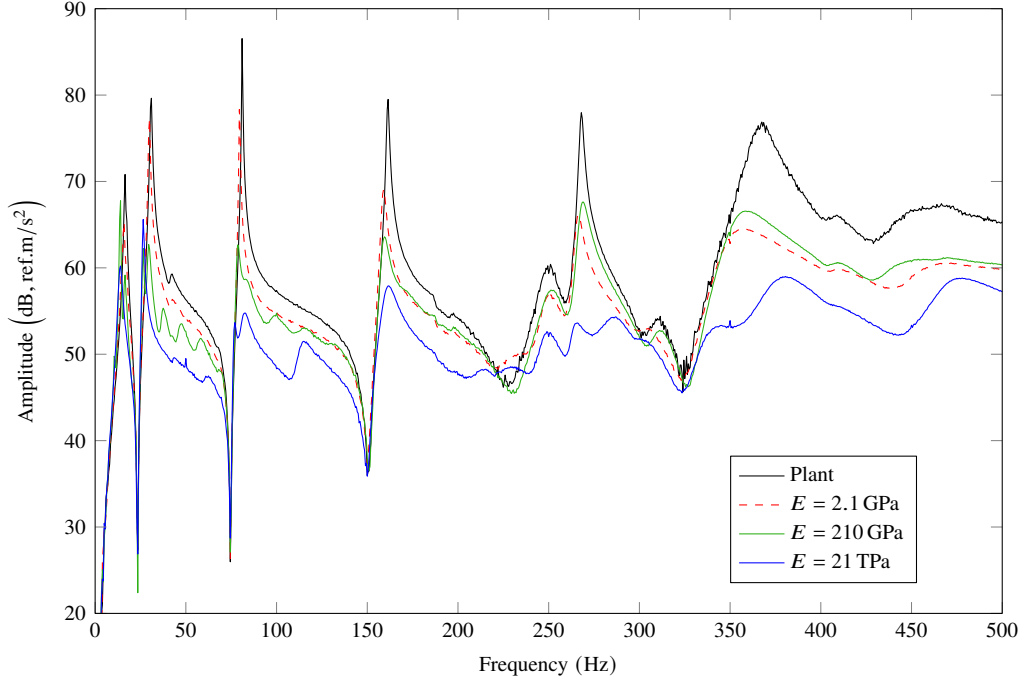


Figure 22: Influence of Young's modulus on ABH performance.

6. Conclusion

This paper proposes the new concept of a VABH which replaces a physical tapered wedge beam (i.e., an ABH) with a digital controller. The controller is designed so as to reproduce the ABH's dynamics at the interface with the host structure. Due to practical limitations, the VABH proposed herein only synthesizes the ABH's transversal dynamics. However, we demonstrated both numerically and experimentally that the resulting VABH exhibits performance and features which are very similar to those of a mechanical ABH. Specifically, our experiments highlighted that all the considered resonance peaks of the cantilever beam including the one below 20Hz were attenuated by at least 11 dB.

Virtualizing the ABH solves important practical issues related to size, fatigue and manufacturing. Moreover, ABHs which could not even be imagined in practice, e.g., ABHs with very high Young's modulus or damping ratios, could be tested during the experimental campaign. The VABH has also its own limitations. First, stability margins must be verified to ensure the stability and robustness of the system. Second, the real-time controller limits the number of poles and zeros of the VABH, forcing us to adopt a Craig-Bampton

reduction approach.

Future research could investigate VABHs applied to more complex host structures, implemented through piezoelectric transducers or VABHs synthesizing the rotational dynamics.

Acknowledgement

This research is supported by a grant from the Belgian National Science Foundation (FRS-FNRS PDR T.0124.21), which is gratefully acknowledged.

References

- [1] M. Mironov, Propagation of a flexural wave in a plate whose thickness decreases smoothly to zero in a finite interval, *Sov. Phys. Acoust.* 34 (1988) 318–319.
- [2] V. V. Krylov, F. J. B. S. Tilman, Acoustic ‘black holes’ for flexural waves as effective vibration dampers, *Journal of Sound and Vibration* 274 (3) (2004) 605–619. doi:10.1016/j.jsv.2003.05.010.
- [3] V. Denis, A. Pelat, F. Gautier, B. Elie, Modal Overlap Factor of a beam with an acoustic black hole termination, *Journal of Sound and Vibration* 333 (12) (2014) 2475–2488. doi:10.1016/j.jsv.2014.02.005.
- [4] L. Tang, L. Cheng, Enhanced Acoustic Black Hole effect in beams with a modified thickness profile and extended platform, *Journal of Sound and Vibration* 391 (2017) 116–126. doi:10.1016/j.jsv.2016.11.010.
- [5] A. Pelat, F. Gautier, S. C. Conlon, F. Semperlotti, The acoustic black hole: A review of theory and applications, *Journal of Sound and Vibration* 476 (2020) 115316. doi:10.1016/j.jsv.2020.115316.
- [6] J. Y. Lee, W. Jeon, Vibration damping using a spiral acoustic black hole, *The Journal of the Acoustical Society of America* 141 (3) (2017) 1437–1445, publisher: Acoustical Society of America. doi:10.1121/1.4976687.
- [7] T. Zhou, L. Cheng, A resonant beam damper tailored with Acoustic Black Hole features for broadband vibration reduction, *Journal of Sound and Vibration* 430 (2018) 174–184. doi:10.1016/j.jsv.2018.05.047.

- [8] A. Keys, J. Cheer, Modified acoustic black hole profile for improved fatigue performance, Internoise conference, 2022.
- 240 [9] H. Li, M. Sécail-Géraud, A. Pelat, F. Gautier, C. Touzé, Experimental evidence of energy transfer and vibration mitigation in a vibro-impact acoustic black hole, *Applied Acoustics* 182 (2021) 108168. [doi:10.1016/j.apacoust.2021.108168](https://doi.org/10.1016/j.apacoust.2021.108168).
- [10] H. Li, C. Touzé, A. Pelat, F. Gautier, Combining nonlinear vibration absorbers and the Acoustic Black Hole for passive broadband flexural vibration mitigation, *International Journal of Non-Linear Mechan-*
245 *ics* 129 (2021) 103558. [doi:10.1016/j.ijnonlinmec.2020.103558](https://doi.org/10.1016/j.ijnonlinmec.2020.103558).
- [11] L. Zhang, G. Kerschen, L. Cheng, Electromechanical Coupling and Energy Conversion in a PZT-Coated Acoustic Black Hole Beam, *International Journal of Applied Mechanics* 12 (08) (2020) 2050095, publisher: World Scientific Publishing Co. [doi:10.1142/S1758825120500957](https://doi.org/10.1142/S1758825120500957).
- [12] H. Li, O. Doaré, C. Touzé, A. Pelat, F. Gautier, Energy harvesting efficiency of unimorph piezoelectric
250 acoustic black hole cantilever shunted by resistive and inductive circuits, *International Journal of Solids and Structures* 238 (2022) 111409. [doi:10.1016/j.ijsolstr.2021.111409](https://doi.org/10.1016/j.ijsolstr.2021.111409).
- [13] L. Zhang, G. Kerschen, L. Cheng, Nonlinear features and energy transfer in an Acoustic Black Hole beam through intentional electromechanical coupling, *Mechanical Systems and Signal Processing* 177 (2022) 109244. [doi:10.1016/j.ymssp.2022.109244](https://doi.org/10.1016/j.ymssp.2022.109244).
- 255 [14] K. Hook, J. Cheer, S. Daley, Control of vibration in a plate using active acoustic black holes, *Smart Materials and Structures* 31 (3) (2022) 035033, publisher: IOP Publishing. [doi:10.1088/1361-665X/ac51ae](https://doi.org/10.1088/1361-665X/ac51ae).
- [15] J. Cheer, K. Hook, S. Daley, Active feedforward control of flexural waves in an Acoustic Black Hole terminated beam, *Smart Materials and Structures* 30 (3) (2021) 035003, publisher: IOP Publishing.
260 [doi:10.1088/1361-665X/abd90f](https://doi.org/10.1088/1361-665X/abd90f).
- [16] K. Hook, S. Daley, J. Cheer, Active control of an acoustic black hole using a feedback strategy, *Journal of Sound and Vibration* 528 (2022) 116895. [doi:10.1016/j.jsv.2022.116895](https://doi.org/10.1016/j.jsv.2022.116895).
- [17] A. J. Fleming, S. Behrens, S. O. R. Moheimani, Synthetic impedance for implementation of piezo-electric shunt-damping circuits, *Electronics Letters* 36 (18) (2000) 1525–1526, publisher: IET Digital
265 Library. [doi:10.1049/el:20001083](https://doi.org/10.1049/el:20001083).

- [18] G. Matten, M. Collet, S. Cogan, E. Sadoulet-Reboul, Synthetic Impedance for Adaptive Piezoelectric Metacomposite, *Procedia Technology* 15 (2014) 84–89. doi:10.1016/j.protcy.2014.09.037.
- [19] C. Sugino, M. Ruzzene, A. Erturk, Design and Analysis of Piezoelectric Metamaterial Beams With Synthetic Impedance Shunt Circuits, *IEEE/ASME Transactions on Mechatronics* 23 (5) (2018) 2144–2155, conference Name: IEEE/ASME Transactions on Mechatronics. doi:10.1109/TMECH.2018.2863257.
- [20] K. Yi, G. Matten, M. Ouisse, E. Sadoulet-Reboul, M. Collet, G. Chevallier, Programmable metamaterials with digital synthetic impedance circuits for vibration control, *Smart Materials and Structures* 29 (3) (2020) 035005, publisher: IOP Publishing. doi:10.1088/1361-665X/ab6693.
- [21] C. Sugino, A. Erturk, Analysis of multifunctional piezoelectric metastructures for low-frequency bandgap formation and energy harvesting, *Journal of Physics D: Applied Physics* 51 (21) (2018) 215103, publisher: IOP Publishing. doi:10.1088/1361-6463/aab97e.
- [22] G. Raze, A. Jadoul, S. Guichaux, V. Broun, G. Kerschen, A digital nonlinear piezoelectric tuned vibration absorber, *Smart Materials and Structures* 29 (1) (2019) 015007, publisher: IOP Publishing. doi:10.1088/1361-665X/ab5176.
- [23] R. L. Forward, Electronic damping of vibrations in optical structures, *Applied Optics* 18 (5) (1979) 690–697, publisher: Optica Publishing Group. doi:10.1364/AO.18.000690.
- [24] N. W. Hagood, A. von Flotow, Damping of structural vibrations with piezoelectric materials and passive electrical networks, *Journal of Sound and Vibration* 146 (2) (1991) 243–268. doi:10.1016/0022-460X(91)90762-9.
- [25] C. Sugino, M. Alshaqqa, A. Erturk, Spatially programmable wave compression and signal enhancement in a piezoelectric metamaterial waveguide, *Physical Review B* 106 (17) (2022) 174304, publisher: American Physical Society. doi:10.1103/PhysRevB.106.174304.
- [26] O. Aklouche, A. Pelat, S. Maugeais, F. Gautier, Scattering of flexural waves by a pit of quadratic profile inserted in an infinite thin plate, *Journal of Sound and Vibration* 375 (2016) 38–52. doi:10.1016/j.jsv.2016.04.034.

- [27] L. Tang, L. Cheng, H. Ji, J. Qiu, Characterization of acoustic black hole effect using a one-dimensional fully-coupled and wavelet-decomposed semi-analytical model, *Journal of Sound and Vibration* 374 (2016) 172–184. [doi:10.1016/j.jsv.2016.03.031](https://doi.org/10.1016/j.jsv.2016.03.031).
- 295 [28] V. Denis, F. Gautier, A. Pelat, J. Poittevin, Measurement and modelling of the reflection coefficient of an Acoustic Black Hole termination, *Journal of Sound and Vibration* 349 (2015) 67–79. [doi:10.1016/j.jsv.2015.03.043](https://doi.org/10.1016/j.jsv.2015.03.043).
- [29] G. Abeloos, L. Renson, C. Collette, G. Kerschen, Stepped and swept control-based continuation using adaptive filtering, *Nonlinear Dynamics* 104 (4) (2021) 3793–3808. [doi:10.1007/s11071-021-06506-z](https://doi.org/10.1007/s11071-021-06506-z).
- 300 [30] A. Preumont, Collocated versus Non-collocated Control, in: A. Preumont (Ed.), *Vibration Control of Active Structures: An Introduction Third Edition*, Solid Mechanics and Its Applications, Springer Netherlands, Dordrecht, 2011, pp. 117–130. [doi:10.1007/978-94-007-2033-6_6](https://doi.org/10.1007/978-94-007-2033-6_6).
- [31] G. F. Franklin, J. D. Powell, A. Emami-Naeini, J. D. Powell, *Feedback control of dynamic systems*, Vol. 4, Prentice hall Upper Saddle River, 2002.
- 305 [32] R. Craig, M. Bampton, Coupling of substructures for dynamic analyses., *AIAA Journal* 6 (7) (1968) 1313–1319. [doi:10.2514/3.4741](https://doi.org/10.2514/3.4741).